J Mater Sci: Mater Electron (2024) 35:565

Enhancement of magnetocaloric effect by partial substitution of Bi in $La_{0.60}Dy_{0.10}Sr_{0.30}Mn_{(1-x)}Bi_xO_3$ manganites ($x = 0$, 0.01, 0.03, and 0.10)

Mustafa Zeki Kurt[1], Selda Kılıç Çetin[1,*], Arda Kandemir[1], Gönül Akça[1], Faruk Karadağ[1], and Ahmet Ekicibil[1]

[1] *Department of Physics, Faculty of Sciences and Letters, Çukurova University, 01330 Adana, Turkey*

Received: 27 September 2023
Accepted: 29 February 2024

© The Author(s), 2024

ABSTRACT

In this study, the effects of Bi substitution for Mn on the magnetic and magnetocaloric properties of $La_{0.60}Dy_{0.10}Sr_{0.30}Mn_{(1-x)}Bi_xO_3$ manganites ($x = 0$, 0.01, 0.03, and 0.10) synthesized using the sol–gel method were investigated. The samples $x = 0$, 0.01, and 0.03 had been indexed in an orthorhombic structure (space group Pnma), while sample $x = 0.10$ had been indexed in a hexagonal structure (space group R3c). The thermomagnetic measurements showed an increase in the Curie temperature (T_C) with increasing Bi content, as well as an increase in magnetization at low temperatures. The T_C values were determined as 322, 318, 327, and 360 K for $x = 0$, 0.01, 0.03, and 0.10 samples, respectively. Maximum magnetic entropy change ($-\Delta S_M^{max}$) values obtained from isothermal magnetization measurements showed an increase with the amount of Bi. The $-\Delta S_M^{max}$ value of 3.80 $Jkg^{-1}K^{-1}$ at 5 T for the $x = 0$ sample increased to 4.12 $Jkg^{-1}K^{-1}$ for the $x = 0.10$ sample with the highest Bi content. From the Arrott curves, it was observed that all samples exhibited a second-order magnetic phase transition. The obtained values of relative cooling power (RCP), which is an important factor in determining the performance of cooling material, are in the range of 282, 262, 251, and 232 Jkg^{-1} for $x = 0$, 0.01, 0.03, and 0.10, respectively.

1 Introduction

The demand for energy is increasing day by day due to developing technology, economic growth, and population expansion. Currently, the energy consumed for cooling and air conditioning constitutes a significant portion, approximately 17%, of global electricity consumption [1]. Therefore, unless the energy efficiency of the air conditioning systems is improved or new technologies are introduced, electricity consumption will increase exponentially. At this point, magnetic cooling systems are considered as a good alternative to current systems. In comparison to existing systems, magnetic cooling systems are expected to be more efficient, environmentally friendly, low noise, and have lower maintenance costs [2–4]. The physical basis of magnetic cooling systems lies in the magnetocaloric effect (MCE). Not only the MCE but also other

Address correspondence to E-mail: kilics@cu.edu.tr

https://doi.org/10.1007/s10854-024-12292-2
Published online: 13 March 2024

effects in magnetic materials have been the subject of research, and various technologies have been developed and used [5, 6]. The MCE is the change observed in the temperature of a material under an adiabatically applied magnetic field [7]. In order to produce a magnetic refrigerator operating at room temperature, the magnetocaloric materials used in the system must meet specific requirements. These materials should have magnetic phase transition temperatures close to room temperature and exhibit significant temperature changes, that is, a large magnetic entropy change, at low magnetic field values. Although there are numerous families of magnetocaloric materials showing a magnetic phase transition around room temperature, perovskite manganites are widely studied for their ability to adjust transition temperatures with different element doping and their low magnetic hysteresis [8]. Perovskites, which have a rich chemical diversity, have also been studied for functional applications such as data storage, energy storage, energy conversion, energy harvesting, and catalysis, apart from magnetic cooling systems based on MCE [9].

La-based manganites have been extensively studied due to their giant magnetoresistance and high magnetocaloric properties at room temperature [8, 10]. In these manganite systems, the substitution of cations at the La site changes the amount of Mn^{3+} ($3d^4$, $t_{2g}^3 e_g^1$) ions to Mn^{4+} ($3d^3$, $t_{2g}^3 e_g^0$) ions. The presence of both Mn^{3+} and Mn^{4+}-mixed valence states in the structure leads to a double-exchange (DE) interaction supporting ferromagnetism. This ferromagnetic interaction occurs because the e_g electrons hop between the d orbitals of these partially filled neighboring Mn ions with the p orbital spacing of the oxygen surrounding the Mn. Therefore, the ratio between these Mn^{3+} and Mn^{4+} ions is one of the important parameters that affect the magnetic transition temperature of the materials. In order to optimize the transition temperature and magnetic entropy change values of the lanthanide manganite materials, numerous studies have been conducted, such as La substitution by different rare-earth cations [11–14] or alkaline elements (IA or IIA groups) [15, 16], and Mn-site substitutions [17, 18]. The magnetocaloric properties of the manganites also may show a variation by different factors such as particle size, material production method, sintering temperature [19], etc. Different element substitution to B-site changes the number of Mn^{3+} and Mn^{4+} ions and may induce a significant disorder in the manganese network [20]. This also causes a variation in the interactions between Mn^{3+} and Mn^{4+} ions. The change observed in the structural properties of a magnetic material by substitution induces a change in its magnetic properties such as magnetic anisotropy and Curie temperature [21]. The effects of substitution have not only been a subject of research for MRS based on the principle of the MCE. In many studies, the effects of substitution on the structural, electrical, and magnetic properties of various materials used in different technological applications such as high-frequency transformers, magnetic memory and microwave electronics devices, etc. have been discussed [22, 23]. Bismuth has recently been the subject of extensive research as an additive element due to its unusual physical qualities [24–27]. In addition, Bi-based materials also have been synthesized with different production methods and investigated for various applications [24–26]. Previous studies revealed that the $La_{0.60}Dy_{0.10}Sr_{0.30}MnO_3$ compound exhibited high MCE at a transition temperature above room temperature [28]. In this study, the effects of post-transition metal Bi substitution for Mn on the transition temperatures and MCE values in $La_{0.60}Dy_{0.10}Sr_{0.30}Mn_{(1-x)}Bi_xO_3$ manganites ($x = 0$, 0.01, 0.03, and 0.10) are investigated.

2 Experimental procedure

2.1 Materials preparation

$La_{0.60}Dy_{0.10}Sr_{0.30}Mn_{(1-x)}Bi_xO_3$ manganites, where $x = 0$, 0.01, 0.03, and 0.10, were produced using the sol–gel method. Initially, appropriate stoichiometric amounts of the starting compounds were determined based on the formulas of the targeted materials. The raw materials ($La(NO_3)_3{\cdot}6H_2O$ (99.999% Aldrich), $Mn(NO_3)_2{\cdot}4H_2O$ (> 97.0% Sigma–Aldrich), Dy_2O_3 (99.9% Sigma–Aldrich), SrO (99.9% Sigma–Aldrich), and Bi_2O_3 (99.999% Aldrich) were used as starting compounds. After accurately weighing the starting compounds with a precision balance, they were dissolved in separate beakers by adding distilled water. Solutions that were insoluble in pure water, such as Dy_2O_3, were made into a homogeneous solution by adding diluted HNO_3. The homogeneously prepared starting solutions were transferred to a single beaker and mixed with a heated magnetic stirrer at 300 °C. To obtain the gel form of the solution, citric acid and ethylene glycol were added in proportions determined

according to the amounts of the starting compounds. Subsequently, to facilitate the removal of the resulting mixture from the beaker, heat treatment was applied 550 °C for 1 h. The calcination process at 600 °C for 6 h was then employed to eliminate the organic compounds added in the initial production stage from the structure. Following calcination, the samples underwent a series of grinding and mixing processes. The ground samples were pelleted with the aid of a hydraulic press and subjected to a sintering process at 1200 °C for 24 h in a cylindrical furnace to crystallize. Finally, they were left to cool in an air atmosphere.

2.2 Materials characterization

The crystallographic characterization was conducted using an x-ray diffractometer (XRD; PANalytical Empyrean) with a CuKα radiation source ($\lambda = 1.5406$ Å). The morphology of the samples was examined using a scanning electron microscope (SEM; FEI Quanta 650 Field Emission SEM) at 20 kV acceleration voltage. Magnetization measurements were carried out with a Quantum Design PPMS Dynacool-9 T magnetometer at magnetic fields ranging from 0 to 5 T.

3 Results and discussions

XRD patterns of $La_{0.60}Dy_{0.10}Sr_{0.30}Mn_{(1-x)}Bi_xO_3$ samples performed at room temperature are given in Fig. 1 for $x = 0$, 0.01, 0.03, and 0.10, respectively. It can be seen from the diffraction patterns that the samples exhibit sharp peaks. In addition, the widths of the peaks are also seen to be narrow based. In this way, the narrow base and sharp diffraction patterns indicate that good crystallization is achieved in the samples. The structural characterization is conducted using the PANalytical X'Pert High Score software to identify candidate phases. Then, the XRD data were analyzed in detail by MAUD software using Rietveld refinement techniques. The observed and calculated patterns by Rietveld refinement are shown in Fig. 1 as a solid rectangle and a solid red line, respectively. The difference between observed and calculated data is represented

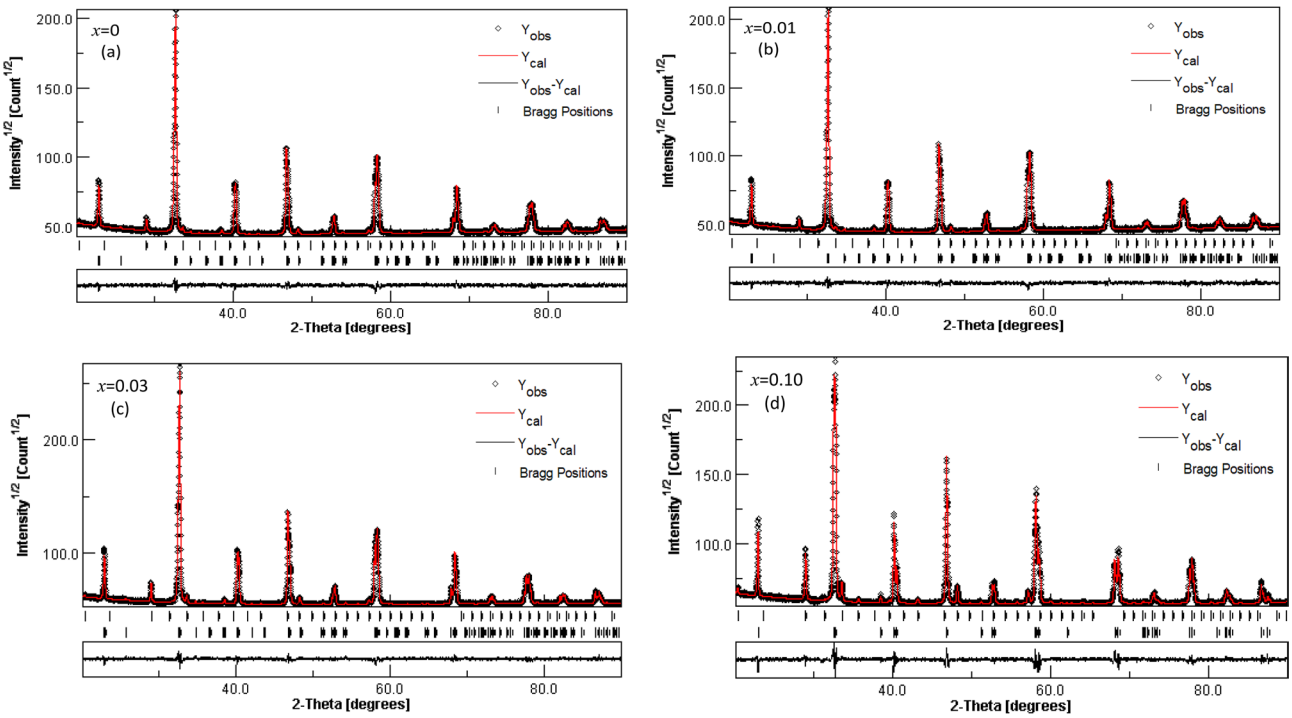


Fig. 1 XRD data and refinement of the $La_{0.60}Dy_{0.10}Sr_{0.30}Mn_{(1-x)}Bi_xO_3$ samples for **a** $x = 0$, **b** $x = 0.01$, **c** $x = 0.03$, and **d** $x = 0.10$. Solid quadrangle, solid red line, solid black line, and vertical ticks indicate observed data, calculated data, the difference between observed and calculated data and Bragg reflections, respectively. Bragg reflections of the Dy_2O_3 phase and main phase are represented in the top and bottom vertical ticks, respectively

by the black line. Bragg reflections of the Dy_2O_3 phase and the main phase are represented in the top and bottom vertical ticks, respectively. The XRD spectra of the samples, except for $x = 0.10$, indicate orthorhombic symmetry with the Pnma space group and contain a very small density of the Dy_2O_3 impurity phase. From the refinement results, the volume fraction of the Dy_2O_3 impurity phase was evaluated as 1.7, 1.4, 2.2, and 5.6% for $x = 0$, 0.01, 0.03, and 0.10 samples, respectively. From the XRD pattern of the $x = 0.10$ sample, it was determined that the crystal structure was hexagonal in the R3c space group. The lattice parameters and unit cell volume values obtained from the refinement are given in Table 1. It is seen that the unit cell volume increases with the increase of Bi substitution in the Mn region. This increase is attributed to the fact that the ionic radius of Bi^{3+} (1.03 Å) added to the structure is larger than that of Mn^{3+} (0.645 Å) [29].

The crystallite size (D) of the samples has been estimated from the most intense diffraction peak using Scherrer's equation given as follows [30]:

$$D_{XRD} = \frac{\kappa\lambda}{\beta cos\theta} \quad (1)$$

where λ is the X-ray wavelength ($\lambda = 1.54060$ Å), κ is the grain shape factor, β is the full width at half maximum of the most intense peak, and θ is the Bragg diffraction angle. The obtained β and D values are given in Table 1. It is seen that the β value decreases with Bi substitution for Mn, and accordingly, the D value increases. This increase can be attributed to the change in the ionic radii of the displaced Mn^{3+} and Bi^{3+} elements and supports the increase in unit cell volumes.

SEM images were obtained to examine the surface morphology of the samples and determine the average particle sizes. Figure 2 shows the SEM images of the parent sample and the Bi-doped sample at $x = 0.10$ concentration at 20 kx magnification. From the SEM images, it is seen that the samples are composed of particles of different sizes and polygonal shapes separated by clear boundaries. In both samples, intergranular spaces are observed in some regions. The average particle size of the samples was determined by ImageJ program. With the addition of Bi to the structure, a decrease in the particle size was observed only for the $x = 0.01$ sample, while particle sizes increased in the other samples. SEM images show that with the addition of Bi, grain boundaries are more distinct, and tight grain structures form in some places. These changes affect magnetic and magnetocaloric results. The average particle size was determined as 0.79, 0.74, 1.04, and 1.16 μm for $x = 0$, 0.01, 0.03, and 0.10 samples, respectively. It is seen that the particle size observed in SEM is larger than the D value observed in XRD. This difference can be attributed to the agglomeration of smaller grains into larger particles [31].

In order to determine the transition temperatures of the compounds, temperature-dependent magnetization measurements, ($M(T)$), were carried out in the 5–360 K temperature range by applying a 250 Oe magnetic field as zero-field cooling (ZFC) and field cooling (FC) processes. Figure 3 shows the $M(T)$ curves of the $La_{0.60}Dy_{0.10}Sr_{0.30}Mn_{(1-x)}Bi_xO_3$ samples for $x = 0$, 0.01, 0.03, and 0.10 at ZFC and FC processes. From the $M(T)$ curves, it is seen that the compounds exhibit a magnetization value at low temperatures, and this magnetization value decreases gradually with increasing temperature. At a certain temperature value, the magnetization decreases sharply, and the magnetization of the material approaches zero. At this point, known as the Curie temperature (T_C), the compounds showed a transition from the ferromagnetic (FM) state to the paramagnetic (PM) state. Below the T_C, moving towards the FM region, the overlap between the ZFC and FC magnetization curves disappears, and a distance between these two curves is observed. This separation may be attributed to magnetic anisotropy and domain-pinning effect [32]. It is also seen from Fig. 3 that this separation between the ZFC and FC curves decreases with the addition of Bi to the structure, which is attributed to the decrease in anisotropy in the material. The dM/dT (T) curves of the samples,

Table 1 Structural parameters of $La_{0.60}Dy_{0.10}Sr_{0.30}Mn_{(1-x)}Bi_xO_3$ ($x = 0$, 0.01, 0.03, and 0.10) samples

Samples	a (Å)	b (Å)	c (Å)	V (Å^3)	β(°)	D (nm)
$x = 0$	5.5117	7.7358	5.4764	233.4995	0.130	64.16
$x = 0.01$	5.4772	7.7367	5.5126	233.5989	0.121	68.94
$x = 0.03$	5.4761	7.7350	5.5153	233.6151	0.108	77.24
$x = 0.10$	5.5010	5.5010	13.3605	350.1256	0.120	69.51

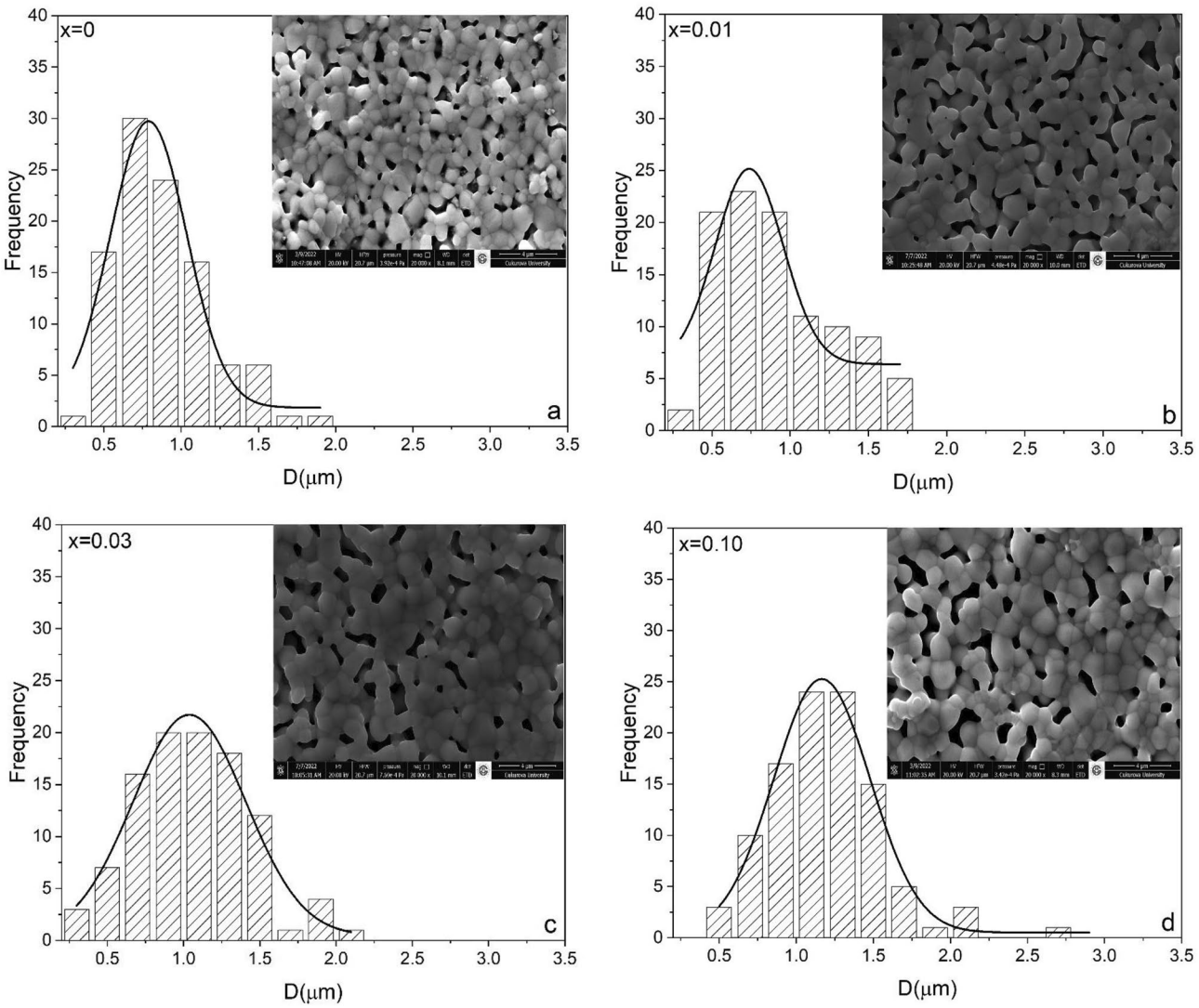


Fig. 2 SEM images at 20 kX magnification and particle size distribution histograms of $La_{0.60}Dy_{0.10}Sr_{0.30}Mn_{(1-x)}Bi_xO_3$ samples for **a** $x=0$, **b** $x=0.01$, **c** $x=0.03$, and **d** $x=0.10$ sample

obtained using $M(T)$curves, are given in the inset graphs in Fig. 3. The T_C values of the samples were determined as the temperature values corresponding to the minimum temperature points of these curves and were found to be 322, 318, 327, and 360 K for $x=0$, 0.01, 0.03, and 0.10 samples, respectively. From the results, it was observed that Bi substitution for Mn generally increased the transition temperatures of the samples, except for the $x=0.01$ sample. The increase in T_C provides evidence of the strengthening of DE interactions, depending on the changes in Mn–O–Mn bond angle and Mn–O bond length with increasing Bi amount [33]. In addition, the increase in T_C with the addition of Bi to the structure is in agreement with the observed increase in particle sizes in SEM images. It is known that decreasing particle sizes lead to increased surface contributions, resulting in various effects on the physical and magnetic properties of the materials [34]. The increase in the amount of surface due to decrease in particle size causes an increase in the ratio of non-magnetic surface layer to magnetic material. Consequently, the increase in particle size with the addition of Bi reveals a decrease in the non-magnetic additive and an increase in the T_C temperature. Based on this, the slight decrease observed in the T_C value of the $x=0.01$ sample can be attributed to the decrease in the average particle size. In addition, it is thought that the Dy_2O_3 impurity phase observed in XRD does

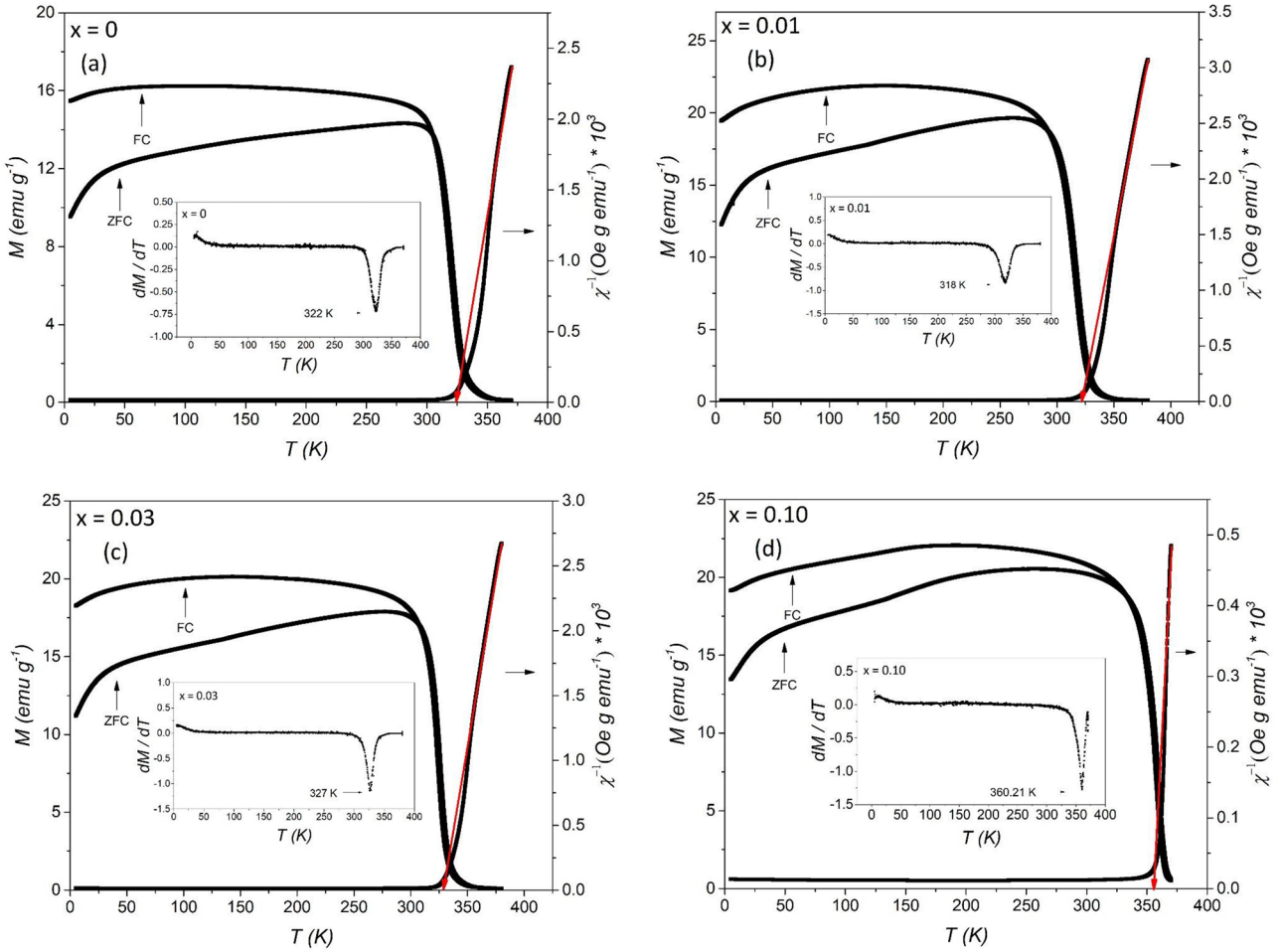


Fig. 3 Temperature-dependent magnetization curves of $La_{0.60}Dy_{0.10}Sr_{0.30}Mn_{(1-x)}Bi_xO_3$ samples for **a** $x=0$, **b** $x=0.01$, **c** $x=0.03$, and **d** $x=0.10$ under 250 Oe magnetic field in the 5–360 K temperature range. Inset figures show (d*M*/d*T*)—*T* curves of the samples

not contribute to the magnetism of the samples since it exhibits a paramagnetic nature above 30 K [35]. The increasing trend observed in the magnetization curve at temperatures below 30 K is thought to be due to the fact that Dy_2O_3 exhibits antiferromagnetic properties under this temperature [36].

It is known that the relationship between susceptibility (χ) and temperature in the PM region should follow the Curie–Weiss law. The temperature dependence of χ^{-1} for the samples is presented in Fig. 3 to see this relationship and obtain information about magnetic interactions. The χ^{-1} (T) curve for the $x=0.10$ sample, which has the highest amount of Bi, shows a linear change as expected in the PM region. However, in other samples, it is seen that the expected Curie–Weiss law on T_C is not adhered to, and there are deviations from linearity. These deviations observed above T_C indicate that this inhomogeneous phase has properties similar to the Griffiths phase, defined by the presence of FM clusters in the PM region [37]. Above the Griffiths temperature (T_G), defined from the maximum of the $d(\chi^{-1})/dT - (T)$ curves, the χ^{-1} (T) curve exhibits linear behavior [38]. T_G values were determined as 350, 345, 349, and 367 K for $x=0$, 0.01, 0.03, and 0.10 samples, respectively. At $T_C < T < T_G$, the magnetic phase of the samples is not pure PM phase and short-range FM clusters occupy in PM matrix. This arises from the distribution of FM spin clusters in the PM region [18]. FM clusters. The difference between T_C and T_G is associated with disorder [20]. It can be seen from the figures that the amount of deviation from linearity decreases with the increase of Bi added to the structure. This can be interpreted as a decrease in the presence of Griffiths phases. In light of this information, it can be stated that the Bi contribution suppresses the formation of Griffiths phases,

causing the FM–PM phase transition to occur in a narrow temperature range.

After determining the T_C values of the samples, isothermal magnetization measurements were made close to these temperatures to obtain the magnetic entropy change, ΔS_M, values related to the magnitude of the MCE. Measurements taken in this particular region provide valuable information about the MCE value since magnetization change rates tend to peak in this region. This means that more information can be obtained by measuring here than elsewhere on the curve. In this study, $M(H)$ measurements were carried out up to a 5 T field value at 4 K temperature steps in these temperature regions of the samples whose transition temperatures were determined. In Fig. 4, $M(H)$ curves of the samples depending on the applied field are given. These curves indicate an increase in the magnetic moment with increasing magnetic fields at low temperatures, followed by saturation when higher fields are applied. This behavior can be attributed to the ferromagnetic ordering within each sample; above its T_C, it behaves like an ideal paramagnet with no net-ordered moments, while below T_C, it shows spontaneous long-range ferromagnetic ordering resulting from interactions between spins within lattice sites due to exchange forces or dipolar coupling mechanisms among them, eventually leading to full-spin alignment along one direction upon the

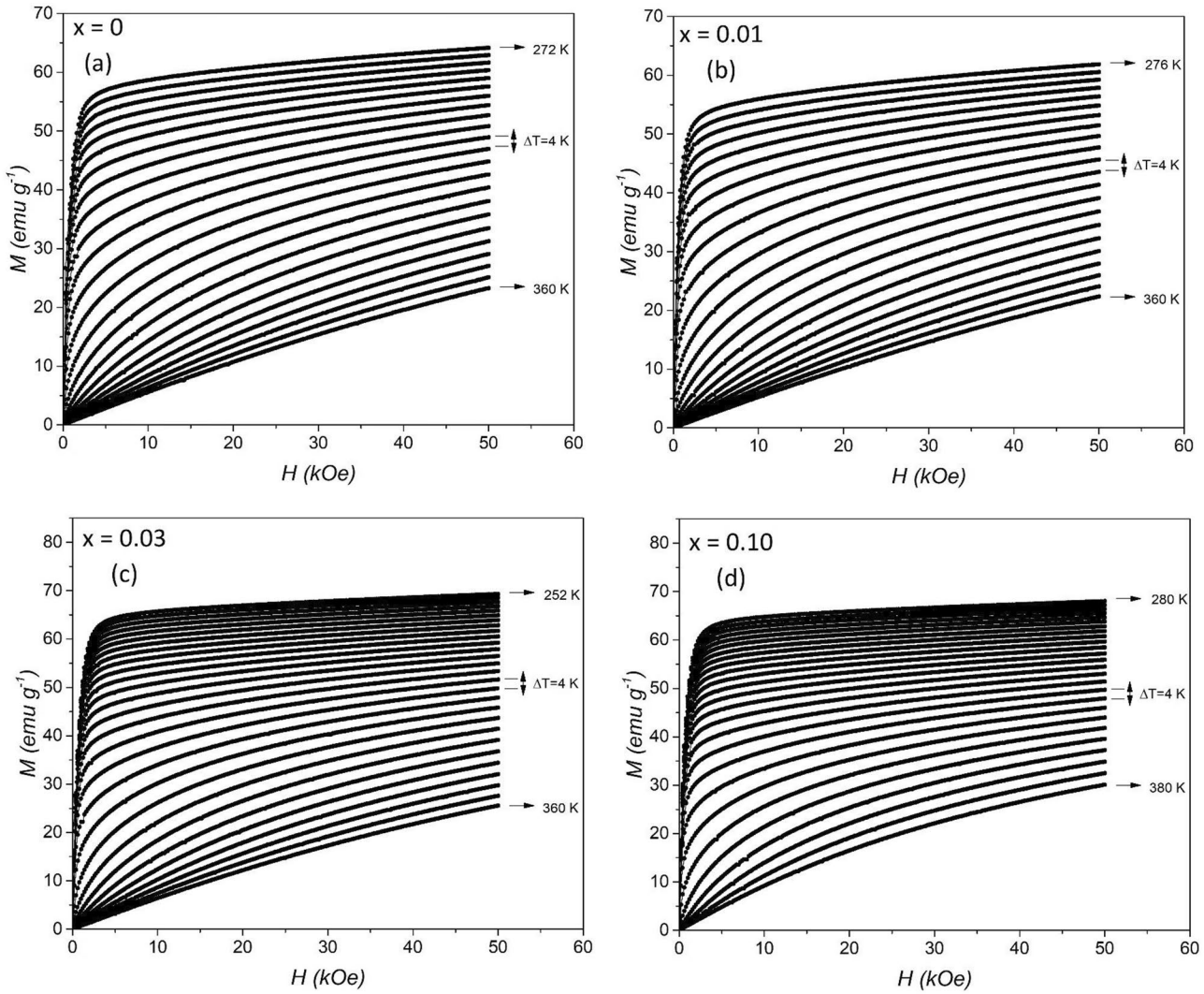


Fig. 4 The isothermal $M(H)$ curves for $La_{0.60}Dy_{0.10}Sr_{0.30}Mn_{(1-x)}Bi_xO_3$ samples for **a** $x=0$, **b** $x=0.01$, **c** $x=0.03$, and **d** $x=0.10$ obtained up to 5 T applied magnetic field in the transition temperature regions at 4 K temperature steps

application of strong enough external magnetic field values, such as those used here (5 T).

The isothermal magnetic entropy change (ΔS_M) is usually determined from isothermal $M(H)$ measurements using the following Maxwell relationship:

$$\left(\frac{\partial S_M(H,T)}{\partial H}\right)_T = \left(\frac{\partial M(H,T)}{\partial T}\right)_H, \quad (2)$$

which directly means that

$$\Delta S_M = \int_0^H \left(\frac{\partial M}{\partial T}\right)_{H'} dH'. \quad (3)$$

Due to the fact that $M(H)$ measurements are made at discrete intervals of temperature and applied magnetic field, Eq. (3) is numerically approximated to

$$-\Delta S_M(H,T) = \sum \frac{M_i - M_{i+1}}{T_{i+1} - T_i} \Delta H_i, \quad (4)$$

where M_i and M_{i+1} are the magnetization values at T_i and T_{i+1} temperature under H_i, respectively.

Figure 5 shows the temperature dependence of $-\Delta S_M$ for all samples under different applied magnetic field values. As expected, the maximum magnetic entropy change values ($-\Delta S_M^{max}$) are obtained around the magnetic phase transition temperatures of the samples. Additionally, it is seen that the $-\Delta S_M^{max}$ values

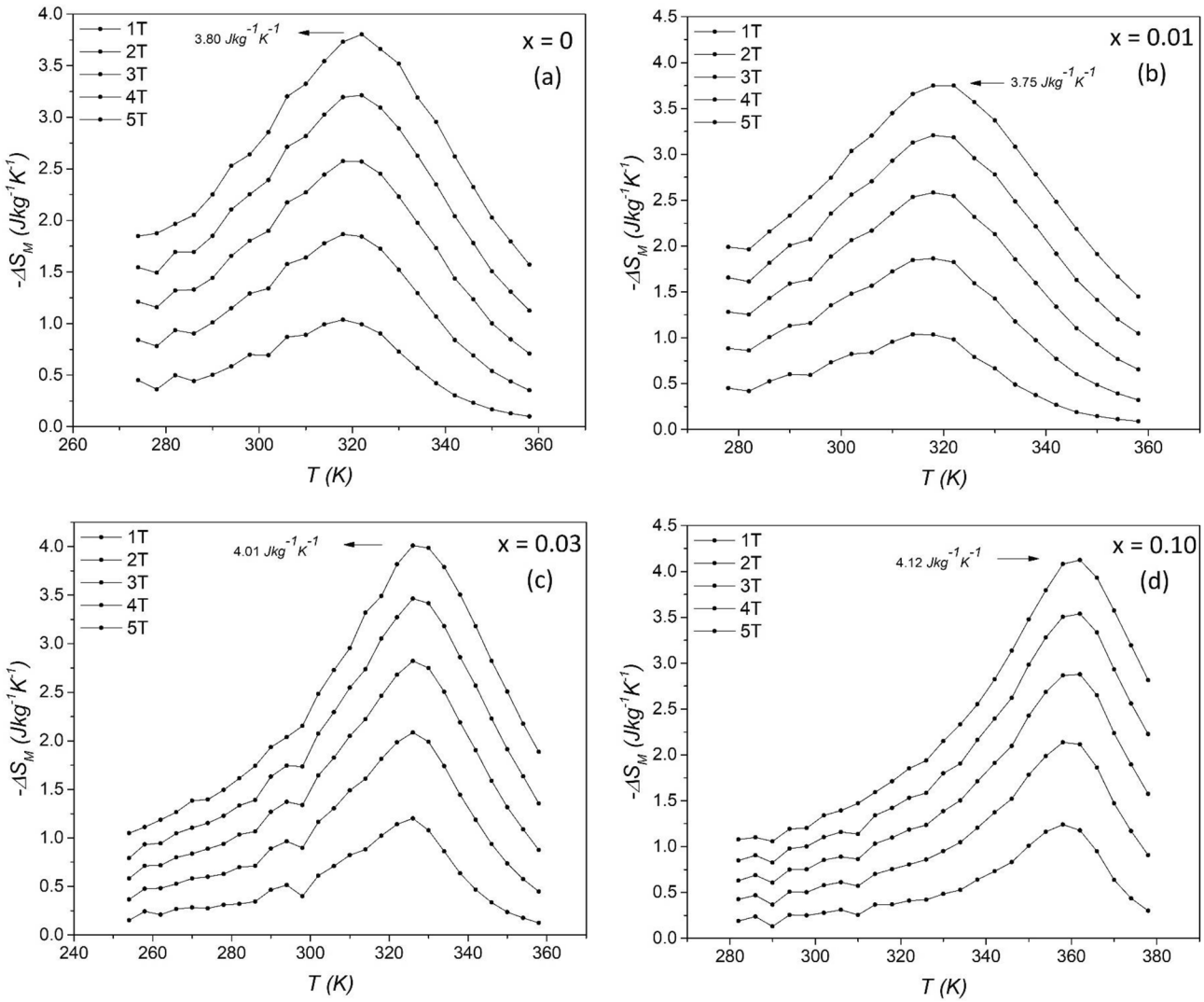


Fig. 5 Temperature-dependent magnetic entropy change curves of $La_{0.60}Dy_{0.10}Sr_{0.30}Mn_{(1-x)}Bi_xO_3$ samples for **a** $x=0$, **b** $x=0.01$, **c** $x=0.03$, and **d** $x=0.10$

increase due to the increase in the magnetization of the samples depending on the applied field value. The $-\Delta S_M^{max}$ values were determined as 3.80, 3.75, 4.01, and 4.12 $Jkg^{-1}K^{-1}$ for $x = 0$, 0.01, 0.03, and 0.10 samples at 5 T, respectively. These values are higher than the values reported for the parent samples in the literature [39, 40]. In addition, Table 2 shows the results of different studies in the literature with different element substitutions for Mn. The results showed that the $-\Delta S_M^{max}$ value increased from 3.8 $Jkg^{-1}K^{-1}$ for the parent sample to 4.12 $Jkg^{-1}K^{-1}$ when 10% Bi was introduced on the Mn-site. This increase in the $-\Delta S_M^{max}$ value is also compatible with the Bi-induced increase in magnetization values. This result indicates that Bi substitution strengthens MCE due to the strong spin–orbit coupling by promoting DE interactions, which also explains the T_C increase. Moreover, the temperature at $-\Delta S_M^{max}$ corresponds to the mean T_C value, which indicates that the system is homogeneous [41]. Based on the fact that, by definition, Maxwell's equations can only be applied correctly if the system is in thermodynamic equilibrium and homogeneous, it is possible to say that the calculations made for the determination of magnetic entropy change values have been verified to be appropriate [41].

Samples showing a second-order magnetic phase transition (SOMT) are desirable for technological applications in cooling systems, as they have negligible magnetic and thermal hysteresis [10]. To determine the nature of the transition in samples, Arrott plots (H/M vs. M^2) converted from the isothermal $M(H)$ data are shown in Fig. 6. The Banerjee criterion allows the type of magnetic phase transition to be determined as SOMT if the Arrott curves have a positive slope around T_C, otherwise FOMT [42]. It is clear from Fig. 6 that all samples exhibit a positive slope in the transition region, indicating that they have SOMT.

Another relevant parameter for the technological applications of cooling systems is the relative cooling power (RCP) values of the materials, which express the amount of heat transferred between hot and cold reservoirs in a thermodynamic cycle [43]. The RCP value is calculated using the following relation [43]:

$$\mathrm{RCP} = \left(-\Delta S_M^{max}\right) \times \Delta T_{FWHM,} \tag{5}$$

where ΔT_{FWHM} is the full width at half maximum of the magnetic entropy change curve. The RCP values calculated using Eq. (5) are provided in Table 2. Although the $-\Delta S_M$ values of the samples increased with the addition of Bi to the structure, a slight decrease was observed in the RCP values. This decrease is attributed to the reduction in the area under the $-\Delta S_M$ curves and, consequently, the decrease in the ΔT_{FWHM} value with the increase in the amount of Bi.

Table 2 Summary of T_C, $-\Delta S_M^{max}$ and RCP values for some studied magnetocaloric samples

Sample	T_C	$\mu_0 H$ (T)	$-\Delta S_M^{max}$ (Jkg^{-1} K^{-1})	RCP (Jkg^{-1})	Refs.
$La_{0.60}Dy_{0.10}Sr_{0.30}MnO_3$	322	5	3.80	282	P.W
$La_{0.60}Dy_{0.10}Sr_{0.30}Mn_{0.99}Bi_{0.01}O_3$	318	5	3.75	262	P.W
$La_{0.60}Dy_{0.10}Sr_{0.30}Mn_{0.97}Bi_{0.03}O_3$	327	5	4.01	251	P.W
$La_{0.60}Dy_{0.10}Sr_{0.30}Mn_{0.9}Bi_{0.1}O_3$	360	5	4.12	232	P.W
$La_{0.67}Dy_{0.03}Sr_{0.3}MnO_3$	264	5	1.05	204	[39]
$La_{0.65}Dy_{0.05}Sr_{0.3}Mn_{0.95}Ti_{0.05}O_3$	175	5	1.79	239	[44]
$La_{0.7}Sr_{0.3}Mn_{0.9}Ti_{0.1}O_3$	210	2	1.45	113	[45]
$La_{0.67}Sr_{0.33}Mn_{0.9}Fe_{0.1}O_3$	266	5	3.3	153	[46]
$La_{0.7}Sr_{0.3}Mn_{0.9}Co_{0.1}O_3$	260	1.5	0.92	54.3	[47]
$La_{0.7}Sr_{0.3}Mn_{0.94}Ni_{0.06}O_3$	324	5	3.90	200	[48]
$La_{0.6}Sr_{0.3}Ca_{0.1}Mn_{0.975}Fe_{0.025}O_3$	312	5	2.18	218.4	[49]
$La_{0.65}Eu_{0.05}Sr_{0.3}Mn_{0.95}Cr_{0.05}O_3$	338	5	4.04	219	[50]
$La_{0.67}Ba_{0.33}Mn_{0.95}Fe_{0.05}O_3$	271	5	2.54	246	[51]
$Pr_{0.67}Ba_{0.33}Mn_{0.95}Fe_{0.05}O_3$	128	5	3.09	287	[51]
$Pr_{0.6}Sr_{0.4}Mn_{0.9}Bi_{0.1}O_3$	255	8	2	–	[52]

*P.W Present Work

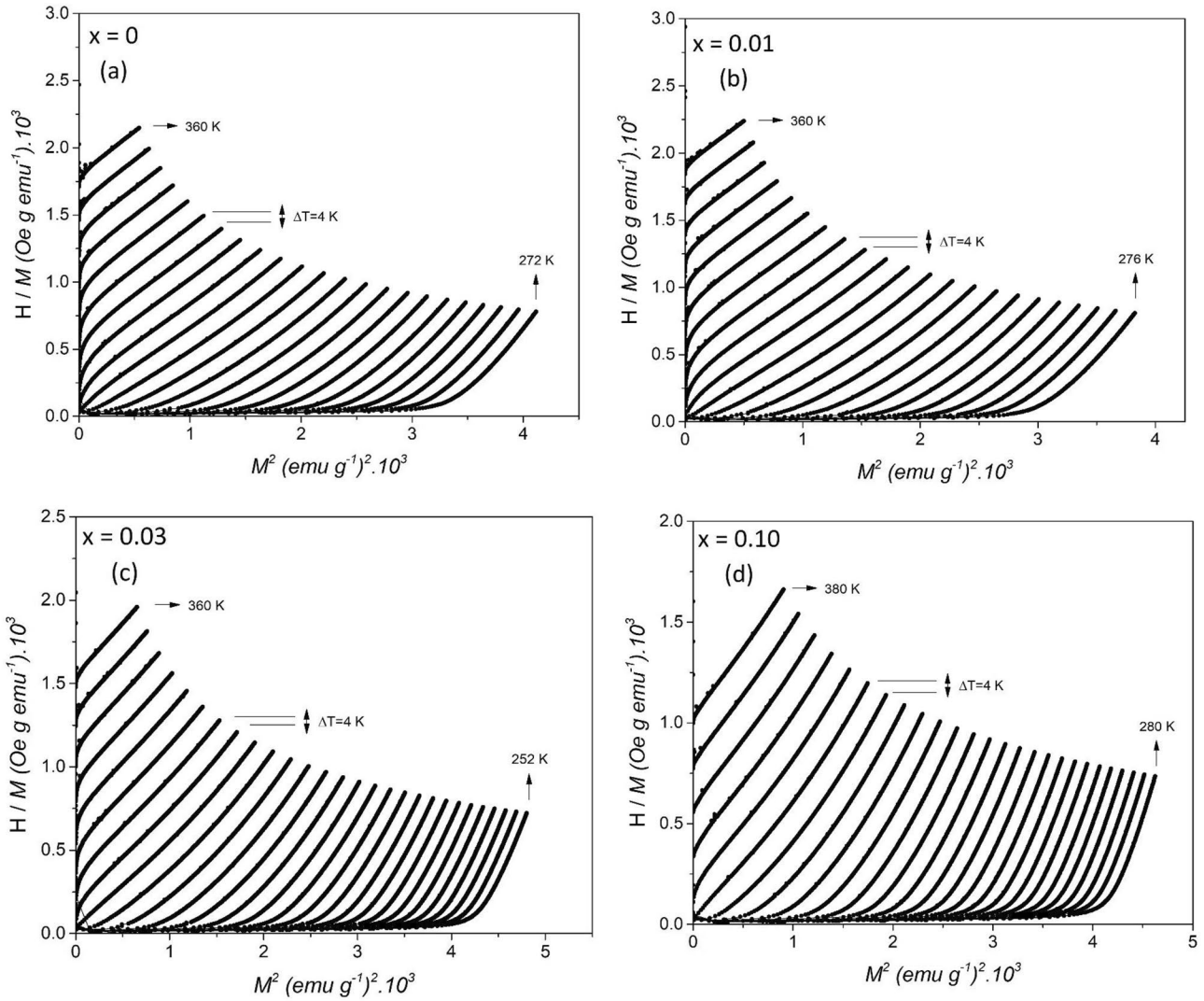


Fig. 6 The Arott plots obtained from the $M(H)$ curves of $La_{0.60}Dy_{0.10}Sr_{0.30}Mn_{(1-x)}Bi_xO_3$ samples for **a** $x=0$, **b** $x=0.01$, **c** $x=0.03$, and **d** $x=0.10$

4 Conclusions

In summary, the effects of Bi substitution for Mn on the structural, magnetic, and magnetocaloric properties of $La_{0.60}Dy_{0.10}Sr_{0.30}Mn_{(1-x)}Bi_xO_3$ manganites ($x=0$, 0.01, 0.03, and 0.10) synthesized by sol–gel method were investigated. XRD results revealed an orthorhombic perovskite structure for $x=0$, 0.01, and 0.03 samples, while the $x=0.10$ sample exhibited a hexagonal structure. The unit cell volume increased with increasing Bi content. Moreover, it is observed that the increase in the Bi doping ratio caused a transformation in the crystal structure. The crystallite size of the samples has been estimated by using Scherrer's equation as 64.16, 68.94, 77.24, and 69.51 nm for $x=0$, 0.01, 0.03, and 0.10 samples, respectively. From SEM images, the average particle size was determined as 0.79, 0.74, 1.04, and 1.16 μm for $x=0$, 0.01, 0.03, and 0.10 samples, respectively, and Bi-substitution to Mn-site caused an increase in the average grain size. It can be seen that the average particle size calculated from SEM images is larger compared to the D value obtained from XRD. This may arise from the agglomeration of smaller grains into larger particles. Thermomagnetic results, at low temperatures, showed an improvement in T_C and magnetization with increasing Bi substitution for Mn. The observed increase in T_C suggests enhanced FM ordering with increasing

Bi content. The results obtained are clear evidence that changes in structural properties affect magnetic properties. Increasing the Bi content has resulted in a higher $-\Delta S_M^{max}$ value compared to the undoped sample. In addition, the magnetic results showed that Bi substitution enhances the magnetocaloric effect due to the strong spin–orbit coupling by promoting DE interactions among magnetic ions. The RCP values, which are important in terms of technological applications, were obtained as 282, 262, 251, and 232 Jkg^{-1} for the $x = 0$, 0.01, 0.03, and 0.10 samples, respectively. The decrease in RCP values with increasing Bi content was associated with the narrowing of the magnetic entropy change peaks. The transformation of broad peaks into narrower peaks for FWHMs is attributed to the observed increase in particle size with the addition of Bi to the structure. From the results obtained, it was determined that the RCP values of the samples varied between approximately 57% and 68% of pure Gd. Arrott plots were employed to analyze the nature of the magnetic phase transition. The results indicated a second-order phase transition for all samples.

Overall, this study provides evidence on how introducing small concentrations of Bi into Mn-site in $La_{0.60}Dy_{0.10}Sr_{0.30}Mn_{(1-x)}Bi_xO_3$ system can lead to improvements in T_C and magnetocaloric effect through strong exchange interactions between neighboring spins within each domain wall region created by Bi substitution. The appreciable enhancement of the magnetic entropy change and T_C with Bi substitution affords a wide operating temperature range for these samples to be used in technological applications, and in this sense, these materials are considered to be good candidate materials for magnetic cooling/heating or power generation systems.

Acknowledgements

This work is supported by the Research Fund of Çukurova University, Adana, Turkey, under grant contract number FBA-2021-14197.

Author contributions

All authors contributed to conceptualization; SKÇ contributed to experimental design; SKÇ carried out measurements; AK and SKÇ contributed to manuscript composition and material preparation; MZK, GA, AE, FK, and SKÇ contributed to writing—review and editing; AE and GA contributed to supervision. All authors have read and agreed to the published version of the manuscript.

Funding

Open access funding provided by the Scientific and Technological Research Council of Türkiye (TÜBİTAK).

Data availability

All data generated or used during the study are available from the corresponding author by request.

Declarations

Competing interest The authors declare that they have no known competing financial interests or personal relationships that could have appeared to influence the work reported in this paper.

Ethical approval Not applicable.

Open Access This article is licensed under a Creative Commons Attribution 4.0 International License, which permits use, sharing, adaptation, distribution and reproduction in any medium or format, as long as you give appropriate credit to the original author(s) and the source, provide a link to the Creative Commons licence, and indicate if changes were made. The images or other third party material in this article are included in the article's Creative Commons licence, unless indicated otherwise in a credit line to the material. If material is not included in the article's Creative Commons licence and your intended use is not permitted by statutory regulation or exceeds the permitted use, you will need to obtain permission directly from the copyright holder. To view a copy of this licence, visit http://creativecommons.org/licenses/by/4.0/.

References

1. D. Coulomb, J.L. Dupont, A. Pichard, *International Institute of Refrigeration* (France, Paris, 2015)
2. A.M. Tishin, Y.I. Spichkin, *The Magnetocaloric Effect and Its Applications*, 1st edn., ch. 11 (IOP Publishing LTD, London, 2003), pp. 351–401
3. V.K. Pecharsky, K.A. Gschneidner Jr., Int. J. Refrig. **29**, 1239–1249 (2006)
4. C. Aprea, A. Greco, A. Maiorino, C. Masselli, J. Phys: Conf. Ser. **655**, 012026 (2015)
5. A.M. Tishin, Y.I. Spichkin, V.I. Zverev, P.W. Egolf, Int. J. Refrig **68**, 177–186 (2016)
6. D.B. Migas, V.A. Turchenko, A.V. Rutkauskas, S.V. Trukhanov, T.I. Zubar, D.I. Tishkevich, A.V. Trukhanov, N.V. Skorodumova, J. Mater. Chem. C **11**(36), 12406–12414 (2023)
7. V. Chaudhary, D.V. Maheswar Repaka, A. Chaturvedi, I. Sridhar, R.V. Ramanujan, J. Appl. Phys. **116**, 163918–163926 (2014)
8. M.H. Phan, S.C. Yu, J. Magn. Magn. Mater. **308**, 325–340 (2007)
9. A. Barman, S. Kar-Narayan, D. Mukherjee, Adv. Mater. Interfaces **6**, 1900291 (2019)
10. V.E. Salazar-Muñoz, A. Lobo Guerrero, S.A. Palomares-Sánchez, J. Magn. Magn. Mater. **562**, 169787 (2022)
11. G. Akça, S. Kılıç Çetin, A. Ekicibil, Ceram. Int. **43–17**, 15811–15820 (2017)
12. S. Skini, S. Ghorai, P. Str¨om, S. Ivanov, D. Primetzhofer, P. Svedlindh, J. Alloys Compd. **827**, 154–292 (2020)
13. M. Chebaane, R. Bellouz, M. Oumezzine, E.K. Hlil, A. Fouzri, RSC Adv. **8**, 7186 (2018)
14. A. Elghoul, A. Krichene, N.C. Boudjada, W. Boujelben, Ceram. Int. **44–11**, 12723–12730 (2018)
15. M. Khlifi, E. Dhahri, E.K. Hlil, J. Appl. Phys. **115–19**, 193905 (2014)
16. I. Messaoui, M. Kumaresavanji, K. Riahi, W. Cheikhrouhou Koubaa, M. Koubaa, A. Cheikhrouhou, Ceram. Int. **43–1**, 498–506 (2017)
17. M. Mansouri, H. Omrani, W. Cheikhrouhou-Koubaa, M. Koubaa, A. Madouri, A. Cheikhrouhou, J. Magn. Magn. Mater. **401**, 593–599 (2016)
18. P.T. Phong, L.V. Bau, L.C. Hoan, D.H. Manh, N. Phuc, L.J. Lee, J. Alloys Compd. **645**, 243–249 (2015)
19. A.O. Ayaş, S.K. Çetin, G. Akça, M. Akyol, A. Ekicibil, Mater. Today Commun. **35**, 105988 (2023)
20. A. Krichene, P.S. Solanki, S. Rayaprol, V. Ganesan, W. Boujelben, D.G. Kuberkar, Ceram. Int. **41**, 2637–2647 (2015)
21. V.E. Zhivulin, E.A. Trofimov, O.V. Zaitseva, D.P. Sherstyuk, N.A. Cherkasova, S.V. Taskaev, D.A. Vinnik, Yu.A. Alekhina, N.S. Perov, D.I. Tishkevich, T.I. Zubar, A.V. Trukhanov, S.V. Trukhanov, Ceram. Int. **49**, 1069–1084 (2023)
22. V.E. Zhivulin, D.P. Sherstyuk, O.V. Zaitseva, N.A. Cherkasova, D.A. Vinnik, S.V. Taskaev, A.V. Trukhanov, Nanomaterials **2**(8), 1306 (2022)
23. V.E. Zhivulin, E.A. Trofimov, S.A. Gudkova, AYu. Punda, A.N. Valiulina, A.M. Gavrilyak, O.V. Zaitseva, D.I. Tishkevich, T.I. Zubar, Zhipeng Sun, S.V. Di Zhou, D.A. Trukhanov, A.V.T. Vinnik, Ceram. Int. **48**, 9239–9247 (2022)
24. A. Fedotov, V. Shendyukov, L. Tsybulskaya, S. Perevoznikov, M. Dong, X. Xue, X. Feng, M.I. Sayyed, T. Zubar, A. Trukhanov, D. Tishkevich, J. Alloys Compd. **887**, 161451 (2021)
25. M.I. Sayyed, A. Askin, M.H.M. Zaid, S.F. Olukotun, M.U. Khandaker, D.I. Tishkevich, D.A. Bradley, Radiat. Phys. Chem. **186**, 109556 (2021)
26. D.I. Tishkevich, A.A. Rotkovich, S.A. German, A.L. Zhaludkevich, T.N. Vershinina, A.A. Bondaruk, I.U. Razanau, M. Dong, M.I. Sayyed, S.V. Leonchik, T. Zubar, M.V. Silibin, S.V. Trukhanov, A.V. Trukhanov, RSC Adv. **13**, 24491 (2023)
27. M.A.I. Zainuddin, N. Ibrahim, Z. Mohamed, J. Solid State Chem. **328**, 124355 (2023)
28. L. Xu, L. Chen, J. Fan, K. Bärner, L. Zhang, Y. Zhu, L. Pi, Y. Zhang, D. Shi, Ceram. Int. **42–7**, 8234–8239 (2016)
29. R.D. Shannon, Acta Cryst. A **32**, 751–767 (1976)
30. A. Bishnoi, S. Kumar, N. Joshi, *Wide-Angle X-ray Diffraction (WXRD): Technique for Characterization of Nanomaterials and Polymer Nanocomposites* (Elsevier, Amsterdam, 2017), pp.313–337
31. W. Mabrouki, A. Krichene, N. Chniba Boudjada, W. Boujelben, Appl. Phys. A **126**, 182 (2020)
32. E. Taşarkuyu, A. Coşkun, A.E. Irmak, S. Aktürk, G. Ünlü, Y. Samancıoğlu, A. Yücel, C. Sarıkürkçü, S. Aksoy, M. Acet, J. Alloy. Compd. **509**, 3717–3722 (2011)
33. M. Koubaa, W.C.-R. Koubaa, A. Cheikhrouhou, J. Alloys. Compd. **479**, 65–70 (2009)
34. R.D. Sánchez, J. Rivas, C. Vázquez-Vázquez, A. López-Quintela, M.T. Causa, M. Tovar, S. Oseroff, Appl. Phys. Lett. **68**, 134–136 (1996)
35. N. Bhakta, A. Das, D. Das, K. Yoshimura, A. Bajorek, P.K. Chakrabarti, Mat. Chem. Phys. **227**, 332–339 (2019)
36. K.P. Shinde, V.M. Tien, L. Huang, S.C. Yu, K.C. Chung, D.H. Kim, J. Appl. Phys. **127**, 054903 (2020)
37. M.B. Salamon, S.H. Chun, Phys. Rev. B **68**, 014411 (2003)
38. P.T. Phong, D.H. Manh, L.C. Hoan, T.V. Ngai, N.X. Phuc, In-Ja Lee. J. Alloy. Compd. **662**, 557–565 (2016)

39. I. Sfifir, A. Ezaami, W. Cheikhrouhou-Koubaa, A. Cheikhrouhou, J. Alloy. Compd. **696**, 760–767 (2017)
40. R. Felhi, M. Koubaa, W. Cheikhrouhou-Koubaa, A. Cheikhrouhou, J. Alloy. Compd. **726**, 1236–1245 (2017)
41. J.S. Amaral, V.S. Amaral, J. Magn. Magn. Mater. **322**, 1552 (2010)
42. B.K. Banerjee, Phys. Lett. **12**, 16–17 (1964)
43. K.A. Gschneidner Jr., V.K. Pecharsky, Annu. Rev. Mater. Sci. **30**, 387–429 (2000)
44. R. Felhi, H. Omrani, M. Koubaa, W. Cheikhrouhou Koubaa, A. Cheikhrouhou, J. Mater. Sci.: Mater. Electron. **30**, 12426–12436 (2019)
45. B. Arayedh, S. Kallel, N. Kallel, O. Peña, J. Magn. Magn. Mater. **361**, 68–73 (2014)
46. C.P. Reshmia, S.S. Pillai, K.G. Suresh, M.R. Varma, Mater. Res. Bull. **48**, 889–894 (2013)
47. P. Zhang, H. Yang, S. Zhang, H. Ge, S. Hua, Physica B **410**, 1–4 (2013)
48. S. Çetin, G. Akça, M.S. Aslan, A. Ekicibil, J. Mater. Sci.: Mater. Electron. **32**, 10458–10472 (2021)
49. M. Baazaoui, J. Khelifi, A. Dhahri, E.K. Hlil, E. Dhahri, M. Oumezzine, J. Supercond. Nov. Magn. **28**, 1217–1225 (2015)
50. R. Bellouz, M. Oumezzine, E.K. Hlil, E. Dhahri, J. Magn. Magn. Mater. **375**, 136–142 (2015)
51. M. Baazaoui, M. Boudard, S. Zemni, Mater. Lett. **65**, 2093–2095 (2011)
52. I. Kammoun, W. Cheikhrouhou-Koubaa, W. Boujelben, A. Cheikhrouhou, J. Alloy. Compd. **452**, 195–199 (2008)

Publisher's Note Springer Nature remains neutral with regard to jurisdictional claims in published maps and institutional affiliations.